Egy. J. Pure & Appl. Sci. 2021; 59(2):75-89

Egyptian Journal of Pure and Applied Science

Investigating the radar scattering response of different land-features in the Greater Cairo area of Egypt, using the full-polarimetric SAR data

R. R. Mohammad [1], A. E. Gaber [2], M. M. Abdeen [1] and A. S. Yahia [3]

[1] *National Authority for Remote Sensing and Space Sciences (NARSS), Geology Department, Cairo, Egypt.*
[2] *Geology Department, Faculty of Science, Port-Said University, Port-Said, Egypt.*
[3] *Physics Department, Faculty of Science, Ain Shams University, Cairo, Egypt.*

ARTICLE INFO

Received 09 December 2021
Accepted 13 February 2022

Keywords
Full polarimetric SAR,
Radar scattering,
Landsat 8,
Mapping,
Great Cairo area,
Egypt.

Correspondence
R. R. Mohammad

E-mail
rabab2020202@yahoo.com

ABSTRACT

The full polarimetric Synthetic Aperture Radar (SAR) data offers plentiful information about the geology, geomorphology, hydrology, land cover and soil classification and therefore helps in assessing their potential for development. In this paper, the full-polarimetric SAR (ALOS/PALSAR L-band sensor) data used for mapping different geological units and land features, which are covering some parts of the Greater Cairo area, Egypt. This paper includes data collection, data interpretation, and a validation tool, as well as methodology and preliminary findings. The ALOS/PALSAR images were extracted, decomposed, filtered and geo-referenced. Unsupervised classification scheme with 5 classes was performed for Radar data using (Wishart H-A-α unsupervised classifier), and it exposed to the supervised classification technique with the assistance of the published geologic and geomorphological maps and the high resolution Landsat images ratio techniques. These five classes are categorized as follows; Urban areas: which covers 22% of the study area, Agriculture: canopy covers 53% of the study area, The Nile: about 73 km of the Nile passing through the study area, and two geological Units, Te (Tertiary, which represents sands and sandstones with clay and marl), and Tp (Tertiary Pliocene, which represents sands, sandstone and gravels). Moreover, the classification accuracy assessment (CAA) was performed for the obtained results using 327 ground control points. The CAA showed classification accuracy around 81.82% with Kappa coefficient of 0.8344. This research shows that using full-polarimetric ALOS/PALSAR data, the land cover and geology of Greater Cairo, Egypt, can be accurately mapped without suffering and wasting time, effort, or facing hazards.

1. Introduction

For decades, multispectral sensor systems like Landsat 8 have provided precise land-surface data sets, making spaceborne remote sensing a valuable technology. Sensors on the Landsat 8 Data Continuity Mission (LDCM) detect the reflectance of the sun's energy on the surface in various wavelengths, including visible and infrared. The active sensor SAR (radio detection and ranging) emits and receives short wavelengths that are significantly longer than those detected by optical devices.

Long-wavelength radar can penetrate clouds, water vapor, dust winds, and rains which would delay the wavelengths of the ordinary space-borne optical and multispectral systems [1,2]. The long-wavelength of radar signals makes it difficult and costly to achieve sufficient resolution in the cross-range direction of

real aperture radar systems due to the length of antennas required. As a consequence, imaging static radar systems is not possible. SAR's concept was to send out radar pulses and store the echoes of these pulses, integrating a scene along the path of the SAR sensor (i.e. synthetic aperture), and then combine these echoes using focusing algorithms. This mixture is done in a logical manner [3].

Geological mapping is needed at various scales and can be done using various methods and content such as; local geophysical surveys, local geochemical investigations, geological surveys and evaluations, remote sensing (RS), strategic mineral assessment, and marine geological surveys. since the beginning of remote sensing technology, this data has been used by geologists for mineral detection and tracking, local mapping, mineral resource exploration, environmental monitoring, and monitoring of oil and gas drains. Remote sensing is a tool that can be used with confidence and efficiency in almost every field of earth science [4-22].

SAR data produce different information from the optical one, which operates in the visible and infrared regions of the electromagnetic spectrum. SAR sensors generate and emit a direct beam pulse of specific radar-frequency energy, and then record higher resolution reflected ones along the terrain that build the SAR data. The physical properties of the surface features dominate the SAR data (for example, surface roughness, geometric structure, and orientation). The SAR sensors can acquire the data day and night without considering the cloud cover rain, or weather status, [23] and produce a technical overview of the radar wave with its surface interactions and applications.

SAR images produce a treasure of geological and mineral information, including lithology, geological structure, and hidden geological features. This is particularly true for meteorite impacts, volcanic deposits, and large faults [24-27]. By using ground-penetrating radar (GPR) or especially the ground Sentinel-1 image we can obtain real time quantitative measurements of the surface deformation. The study of Sentinel-1 data has become an important work for national and international organisation engaged in seismic science, disaster assessment, and civil defense. The following are the key guidelines for analyzing earthquakes using Sentinel-1 data: (a) the detection and evaluation of hypocentres [28]. (b) the detection and evaluation of secondary disasters (for example, earthquakes, surface fractures, landslides, mudslides, and surface collapses) [29]. (c) Estimating the seismic sequences' short-term spatial evolution [30]. In recent years, SAR monitoring of surface deformation and geological hazards has become a major concern [31]. This system has been widely used in mine surface monitoring, urban surface monitoring, mine surface monitoring, dam peripheral surface monitoring, and other geological conditions due to its suitability for large-scale ground deformation. Table in [32] summarize recent studies that manipulate SAR data with spatial resolutions greater than 10 m.

In this study, the full-polarimetric SAR ALOS/PALSAR L-band sensor data was integrated with the Landsat 8 data to run supervised and unsupervised classifications for mapping the different geological units and land features covering some parts of the Greater Cairo area.

1.1 The study area

The study area is 1,912 km2, with a 190 km perimeter. And is located in the upper centre of Egypt with Upper Left Latitude 30.112, Upper Left Longitude 31.062, Upper Right Latitude 30.158, Upper Right Longitude 31.329, Lower Left Latitude 29.549, Lower Left Longitude 31.195, Lower Right Latitude 29.596, and Lower Right Longitude 31.46, Fig. **1**.

The oldest exposed rocks in this study area date to the Late Eocene, and they are represented by the Maadi Formation and Anqabiyah Formation that appear in the southern part and two outcrops of Gabal Anasuri and Gabal El-Anqabiyah Fig. **2**. According to [33] Claystone and marls are characteristic of the Upper Eocene east of Cairo City. The Oligocene sediments overlie the Upper Eocene rocks and consist of the Gabal Ahmar Formation which is made up of sandstones and gravels with silicified pipes and tree trunks. The Gabal Ahmar Formation represents a wide area, Formation, Oligo-Miocene basalt flows cover the Oligocene sediments in some parts and they are scattered in some localities, mainly close to the Cairo-Suez highway Fig. 2. The exposed Miocene rocks in the study area are categorised as Middle Miocene marine deposits (Homath Formation), and Upper Miocene non-marine deposits (Hagul Formation), [34].

The study area is from the late Pleistocene, which is represented in the valley by Neonile deposits that are lowering their course at a rate of 1m/1000 years [35] and represented in the eastern desert margin by rock formations that are Eocene, Pleistocene, and Holocene Fig. 3. These are the most numerous, and they cover a large portion of Cairo City's eastern outskirts. Eocene rocks are generally composed of bedded Carbonates and Calistics in varying proportions, alternating with marl and shale. The fractures, joints, and bedding planes play an important role in the frequency of rockfall in this area.

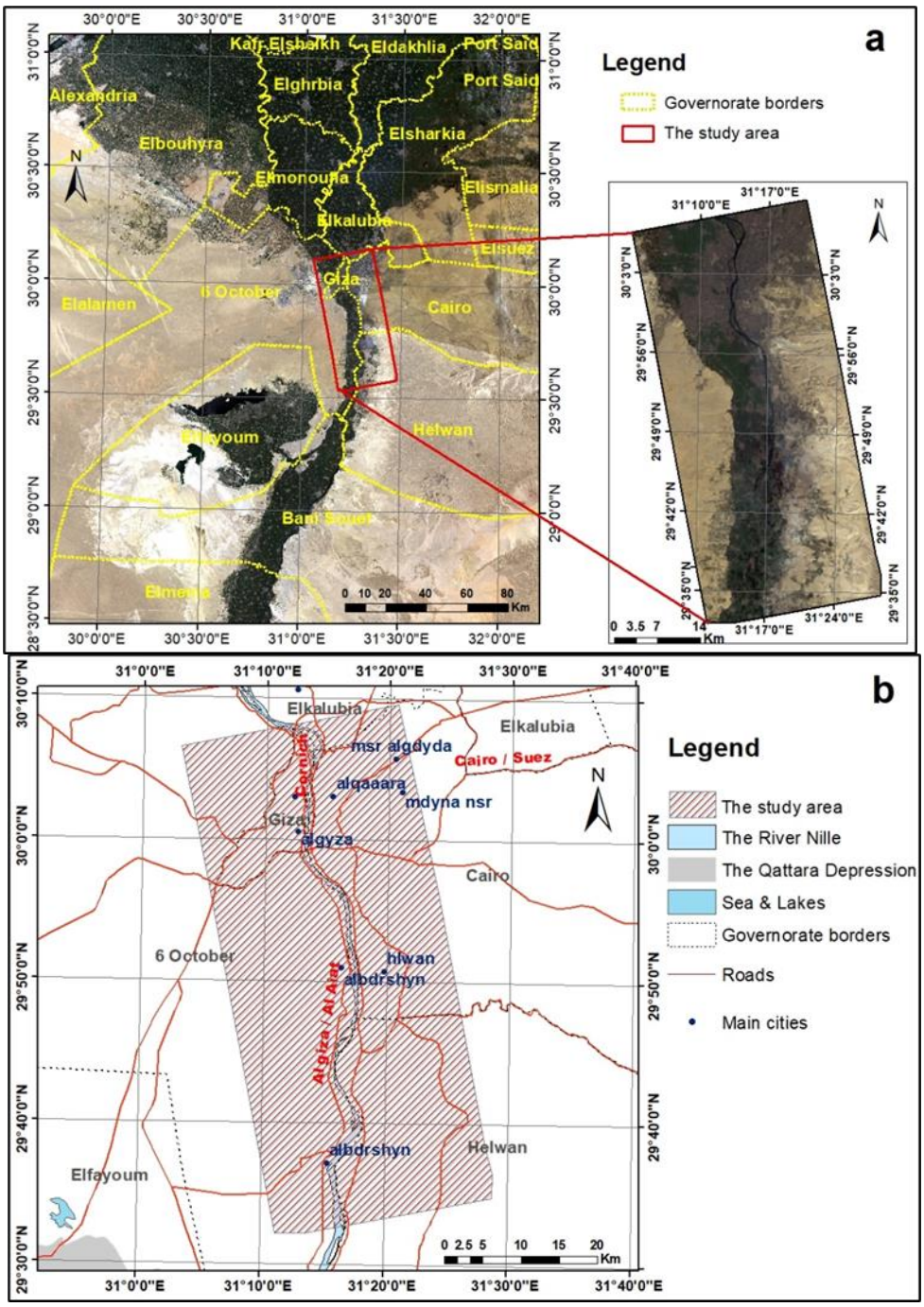

Fig. 1 Location map of the study area, a: Landsat 8 Satellite Image, b: Basemap of the study area

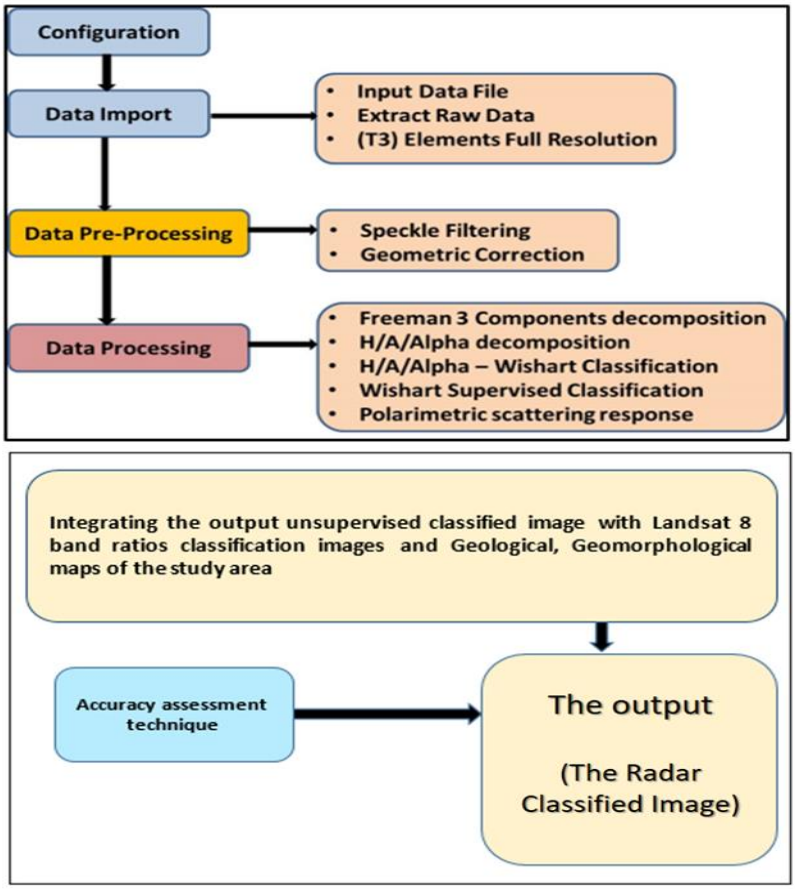

Fig. 2 Flow chart showing the pre-processing and processing steps for polarimetric segmentation of the radar data of the study area

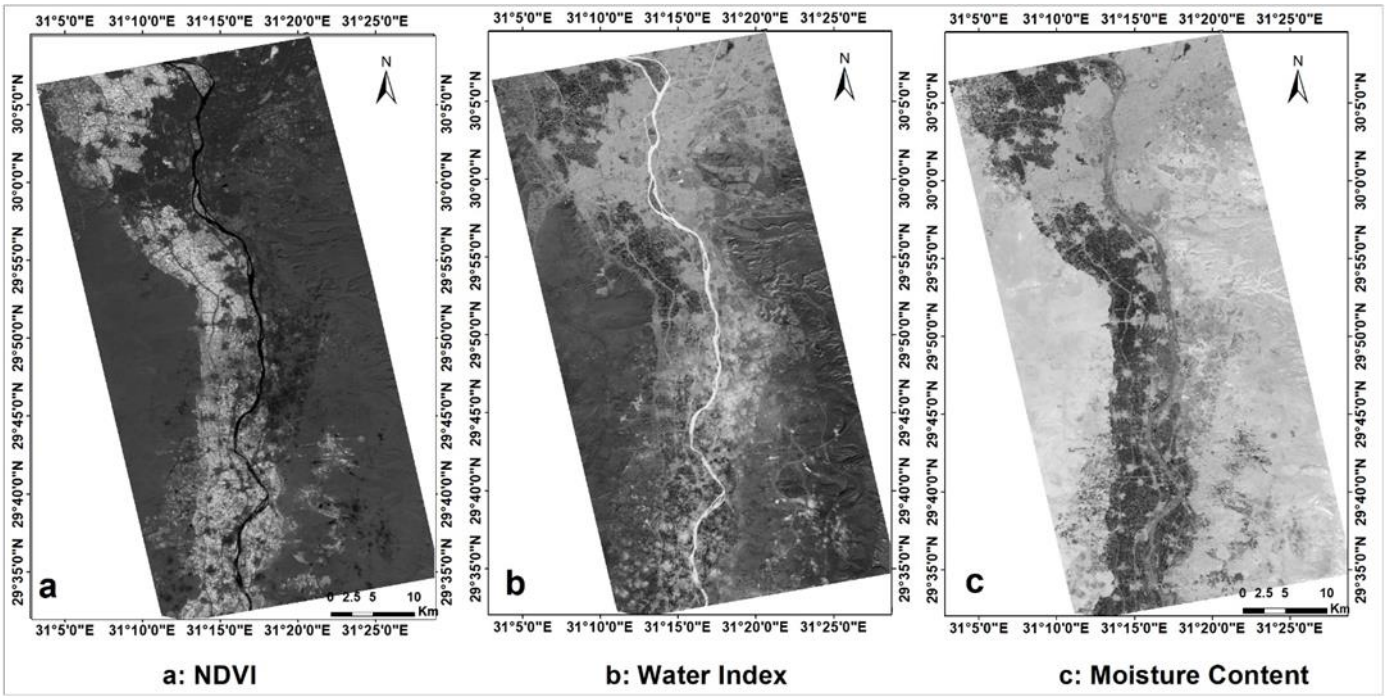

Fig. 3 Landsat 8 satellite image band ratio calculations for the study area, a: represents the NDVI (Normalized difference vegetation index), NDVI=(NIR-Red), b: represents the water index, NDWI=(NIR-MidIR)/(NIR+MidIR), c: the moister stress

2. Materials and methods

In this study, as shown in Fig. 2 four different sources of data: the ALOS/PALSAR image, Landsat 8, geology, and geomorphology maps of Greater Cairo were used and processed. The ALOS/PALSAR is a satellite that carries L-band SAR (Synthetic Aperture Radar) sensor with a wavelength of 0.2360571 m. The used radar image was acquired on May 24, 2007 with the standard quad-pol (Fine) mode (i.e. Fully polarimetric) with "CEOS" format and data level 1.1, SLC mode (Single Look Complex mode) with ascending direction, the backscatter is received in the four polarimetric polarizations (HH, HV, VH, and VV), The nominal azimuth resolution is 4.5 m, the nominal slant range resolution is 9.5 m, and the incidence angle of the image centre is 23.846°.

In addition, the Landsat 8 satellite image band ratio calculations were used to be compared with the radar classified data, Fig. 3. Different image processing techniques were used to enhance the Landsat 8 image and distinguish between the various land covers along the study area. Resolution merge, false color composition (FCC), and principal component analysis (PCA) are examples of these techniques. In the FCC image band-3, band-5, and band-7 in RGB were used. Water bodies and urban areas were mapped using Band-3 (Blue), while the vegetation cover was mapped using Band-5 (NIR), and rock units were mapped using Band 7 (MIR). The spatial resolution of the image (panchromatic image) was improved by combining the spectrum information of lower spatial resolution image (multi-spectral image) with that of the high spatial resolution image [35].

The geology and geomorphology maps of Cairo were mapped and compared to the obtained classified image Fig. 4 & 5.

The Landsat-8 image was enhanced to distinguish between different land covers and geological units. The Arc GIS and ERDAS IMAGINE (2014) softwares were used to help interpret and compare the results with those obtained using the ALOS/PALSAR image.

The PolSAR Data Processing and Educational Toolbox (PolSARpro) was used in this study, along with the free softwares SNAP, ERDAS Imagine, ArcGIS, and NEST.

Furthermore, the Freeman three-components decomposition was used to observe the three components of the scattering mechanism and construct the T3 matrix [36] along the Greater Cairo research region, which is a technique for fitting physically-based decompositions. The 3×3 coherency matrix (T3) is considered the most important matrix, measured by radar system, and it can be written as the following:

$$T_3 = \frac{1}{2}\begin{bmatrix} |S_{hh}+S_{vv}|^2 & (S_{hh}+S_{vv})(S_{hh}-S_{vv})^* & 2(S_{hh}+S_{vv})S_{hv}^* \\ (S_{hh}-S_{vv})(S_{hh}+S_{vv})^* & |S_{hh}-S_{vv}|^2 & 2(S_{hh}-S_{vv})S_{hv}^* \\ 2S_{hv}(S_{hh}+S_{vv})^* & 2S_{hv}(S_{hh}-S_{vv})^* & 4|S_{hv}|^2 \end{bmatrix}$$

Shh and Svv denote co-polarized complex scattering amplitudes, respectively; Shv and Svh denote cross-polarized complex scattering amplitudes.

This T3 matrix can be averaged to reduce the noise and enhance the classification accuracy at the expense of spatial resolution [37], then it can be georeferenced and filtered with the Lee refined filter.

Moreover, the polarimetric target decomposition, Pauli RGB, and Wishart unsupervised classification were used to distinguish and map the various surface sediments and rock units in order to extract and characterize the different scattering responses of the different land covers and geological units, we used the H / A / α algorithm as an unsupervised classification algorithm that it was evolved as shown in Fig. 5, terrain classes can cause feature clustering in the H / α plane. The observable alpha values for a given entropy are limited by curves I and II because the averaging of the many scattering mechanisms limit the range of potential values as the entropy grows (i.e. the shaded areas are not valid). This is due to the fact that as entropy increases, the averaging of the various scattering processes narrows the range of possible values. The H / α plane is a useful representation of the information in the coherency matrix since H and α are both invariant to the type of polarization basis utilized.

When the entropy is high, the ability to distinguish various scattering mechanisms is severely restricted, as shown by the bounds in Fig. 6 (Curves I and II). Cloude and Pottier have suggested an initial partition into 9 classes (8 usable) [38], the classes that were chosen based on general scattering mechanism properties rather than a specific set of data.

unsupervised signal classification, which is based on signal physical properties. Cloude and Pottier's proposed class interpretation is as follows (for more information, see [39, 40]):

- Class Z1: high entropy double-bounce scattering,
- Class Z2: high entropy multiple scattering (e.g. forest canopy),
- Class Z3: high entropy surface scattering,
- Class Z4: medium entropy multiple scattering,
- Class Z5: medium entropy vegetation (dipole) scattering,
- Class Z6: medium entropy surface scattering,
- Class Z7: low entropy multiple scattering (double or even bounce scattering);
- Class Z8: low entropy dipole scattering (strongly correlated processes with a significant amplitude imbalance between HH and VV); and
- Class Z9: low entropy surface scattering (e.g. Bragg scatter and rough surfaces),

This classification method is unaffected by training data sets since it is focused on physical scattering properties. The number of classes required, as well as the method's usability, are determined by the implementation. [41] suggests a small improvement in the class boundaries as well as a new understanding of the grades.

Different forms of surface scattering have been distinguished using the third variable of polarimetric anisotropy. In the H/A plane depiction of surface scattering given in Fig. 7, the shaded area is not possible. A diagonal coherency matrix with minor eigenvalues of 2 and 3, and three ranging from 0 to λ 2, can be used to measure the line circumscribed by the relevant field.

According to [42], classification techniques can be categorized into three main categories: Per-pixel (or pixel-based) classification techniques (for instance, Maximum likelihood, Minimum distance, Isodata, K-means), Sub-pixel classification techniques (for instance, Spectral mixture analysis), and per–field (or object-based) classification techniques.

Generally, in land cover classification, per-pixel classification techniques are the most widely used techniques, in spite of the existence of mixed pixels, which has been identified as a major issue affecting the accuracy of per-pixel classification results, particularly with medium and coarse spatial resolution data [43]. When using coarse spatial resolution data, sub-pixel classification approaches can be more effective than per-pixel approaches in dealing with the mixed pixel problem and providing an accurate estimation of the area of land cover. For fine spatial resolution data, per-field (or object-based) classification approaches perform better than per-pixel classification approaches [44,45].

Several automated methods for classifying Earth Observation (EO) data into featured categories have been established over the last two decades, including Maximum Likelihood (ML), Decision Trees, which take into account the necessary Probability Density Functions, and Neural Networks (NN) which have been shown to be the most beneficial. In this field, non-parametric algorithms based on Support Vector Machine theory have recently been proven to be extremely efficient. We must acknowledge that, in the long run, ML (Maximum Likelihood) and NN (Neural Networks) methods have evolved from a pixel-based to a conceptual (i.e, pixel neighbourhood information) approach made by taking into account, Markov Random Fields (MRF), for example, a versatile technique for modeling spatial dependency [46].

3. The Results and Discussion

The results of an unsupervised identification of a scattering system using H, A, and are used to initialise the unsupervised segmentation scheme shown in Fig. 8. This initialization creates eight reliable clusters that are connected to the physical scattering mechanism. The ML Wishart segmentation, the Unsupervised Wishart H-A-segmentation, has been enhanced by including anisotropy information during the segmentation process. In Fig. 8, anisotropy denotes the relative importance of secondary processes arising from a coherency matrix's expansibility. This polarimetric indicator is especially useful for identifying scattering processes with similar intermediate entropy values but different eigenvalue distributions.

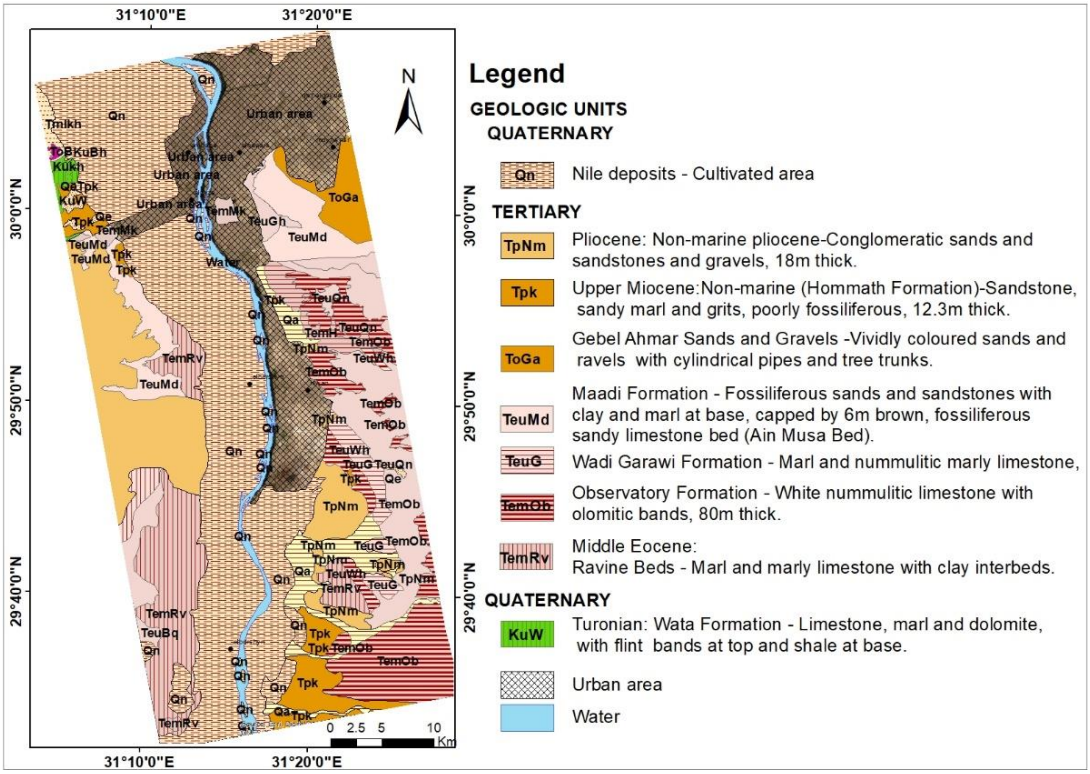

Fig.4 Geological map of the study area (modified after EGSMA, 1990)

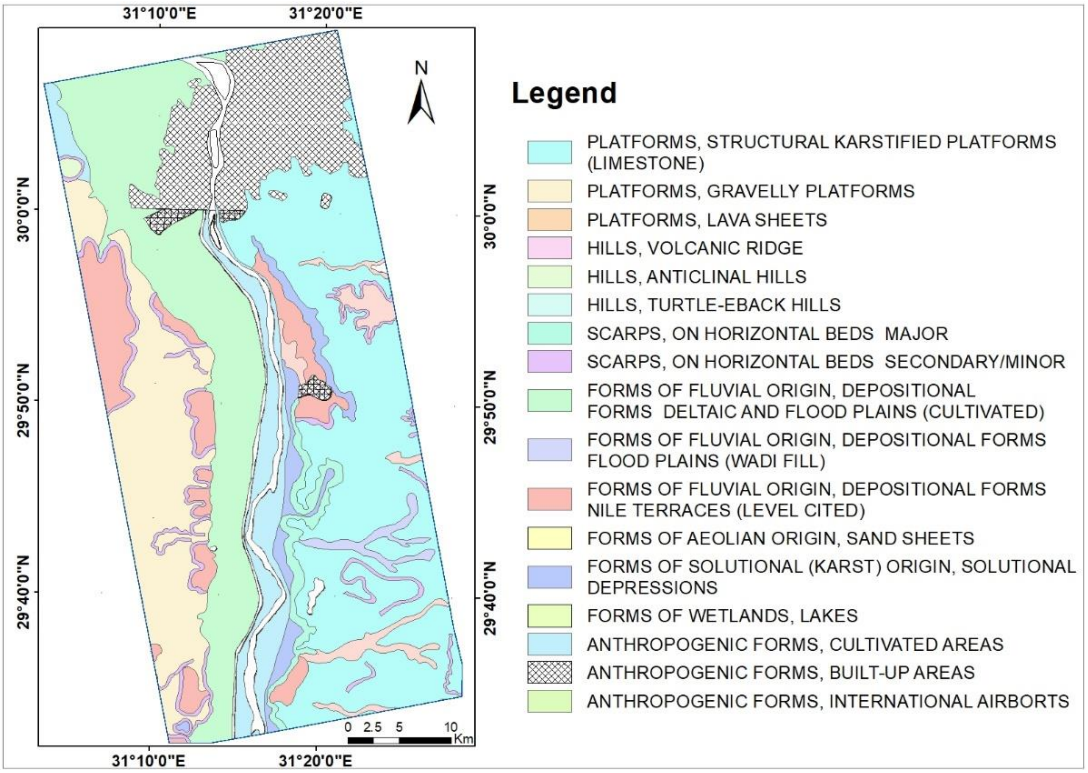

Fig. 5 Geomorphological map of the study area, 2005 EGSMA, NARSS, UNDP, UNESCO

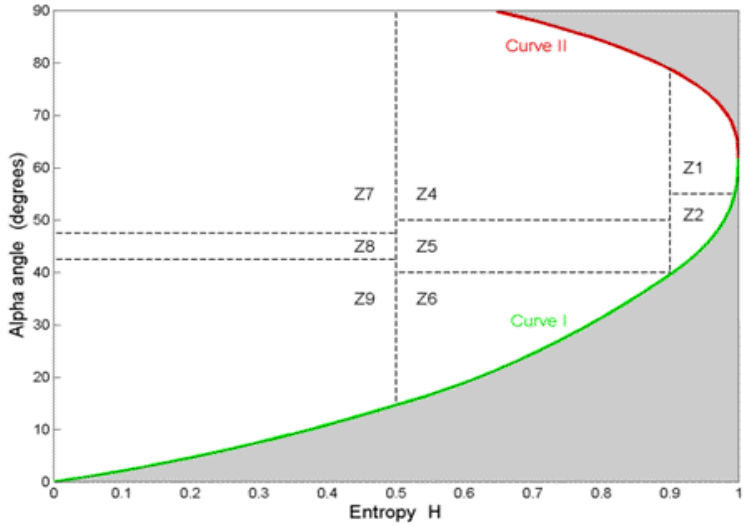

Fig.6 The H/α plane showing the model-based classes and their partitioning. A description of the classes (Z1-Z9) is given in the text, [37]

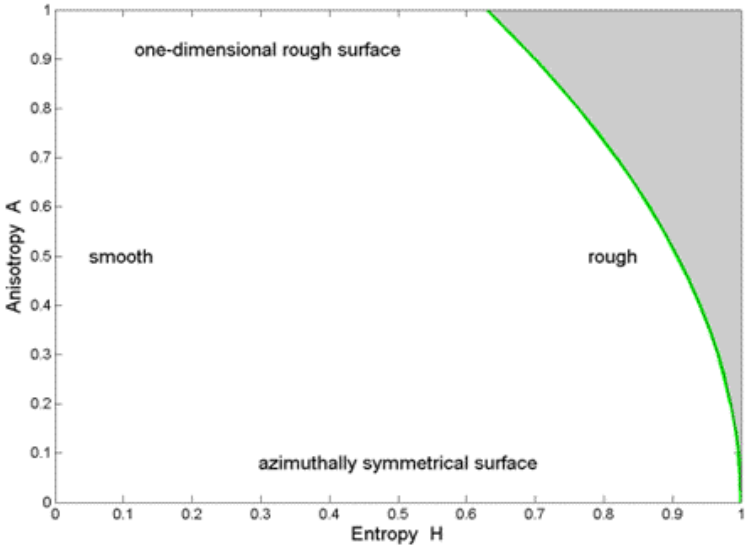

Fig. 7 Types of surface scattering in the Entropy/Anisotropy plane

A high anisotropy value denotes two prevalent scattering mechanisms of equal probability and a small third mechanism, whereas a low anisotropy value denotes a prevalent first scattering mechanism and two non-negligible secondary mechanisms with equal significance. Among the various methods studied, applying two consecutive segmentation procedures, as shown in Fig. 9, is the most effective way to incorporate anisotropy information into the classification algorithm.

First, using the algorithm described in the previous paragraph, the polarimetric data is segmented. After this process was completed, the 8 resulting clusters were divided into 16 by comparing the anisotropy of each pixel to a 0.5 threshold. After that, the 16 segments are used to begin a new Wishart ML segmentation process.

The use of anisotropy in the clustering process helps us to split large segments into smaller clusters, allowing us to discriminate minor inequalities more precisely, as seen in Fig. 10, which shows the improved description of our data's classified scene. The agricultural canopy is constructed from the rest of the forest canopy. Buildings differ from other forms of urban scatterers, much as the Nile and other geological units differ from other surfaces. The Wishart H-A classification scheme divides pixels with similar statistical properties into segments, but it gives no information about the scattering mechanism that each cluster employs.

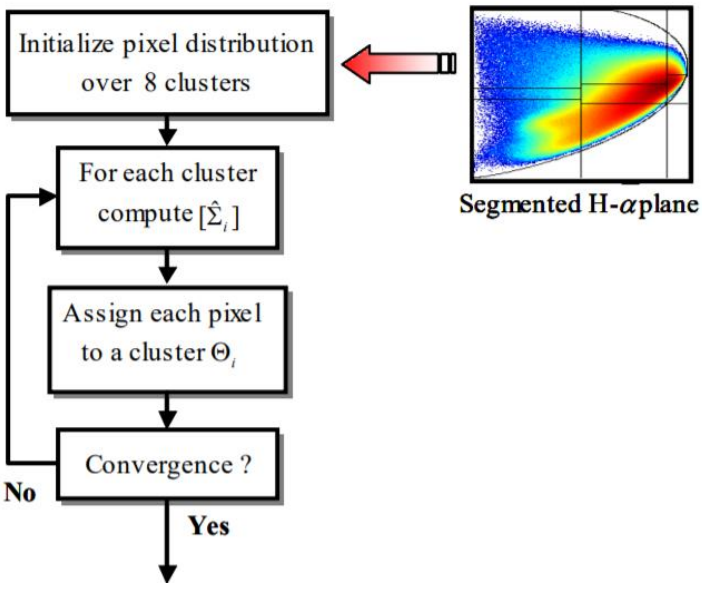

Fig. 8 Unsupervised Wishart H-α segmentation scheme

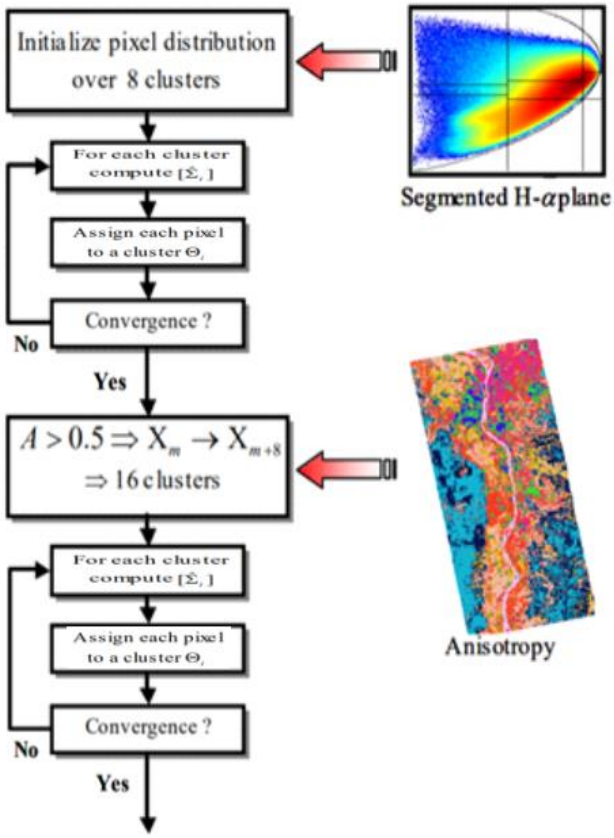

Fig. 9 Unsupervised Wishart H-A-α segmentation scheme

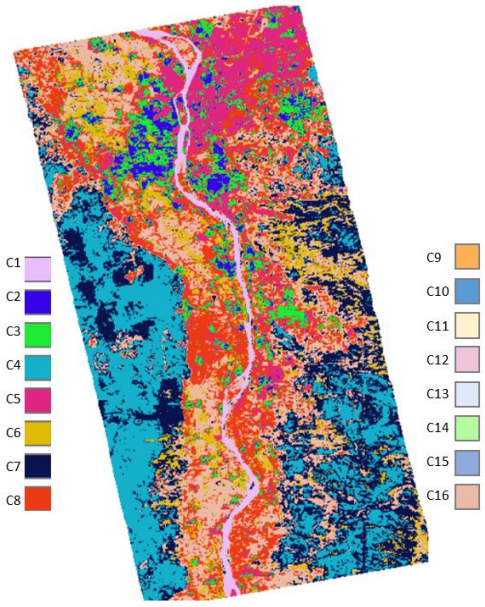

Fig. 10 Wishart H-A-α segmentation

To investigate the accuracy of the classification technique, the integration of the output unsupervised classified image with Landsat 8 band ratio classification images Fig. 3, geological and geomorphological maps of the study area was performed Fig. 4 & 5. Fig. 2 shows the flowchart of the methodology used in this study.

Today, the validation process, also known as accuracy assessment is an essential and integral part of most mapping projects, especially those involving remotely sensed data [47]. To obtain genuinely useful and efficient remotely sensed data, we must use an appropriate accuracy assessment technique. Where the accuracy is determined by comparing a map made from remotely sensed data to another map made from a different source (the reference one). It is determined to what extent the current map generated from remotely sensed data matches the reference map [48].

The creation of the error matrix is the key element of the accuracy assessment, especially the quantitative accuracy assessment, where the error matrix is a square array of numbers arranged in rows and columns representing the number of sample units (i.e. pixel, clusters of pixels, or polygons) related to a specific category in comparison to the actual category as stated by the reference data [49]. Where the ERDAS Imagine "Accuracy Assessment" module was used to select the sample points randomly, which recorded the image class for each point in this sample automatically, we used the viewer to determine the reference class for each point. At the moment we entered the reference class for each sample point, we used Imagine to construct the error matrix and derive some accuracy estimates.

To assess inter-rater reliability, the kappa statistic was used. The rater reliability is important because it indicates the degree to which the classification or data obtained in the study are correct [50], The scale of Kappa value interpretation is as follows.

Finally, as we see, a final unsupervised classification scheme with 5 classes was performed. The unsupervised classification map was converted to supervised classification using the high-resolution Landsat 8 classified images and the published geological and geomorphological maps, as well as field investigation, as discussed in the methodology.

These five classes are categorized as follows; Urban areas: which covers 22% of the study area and represented in red in the final map, Agriculture canopy: which is represented in green, covers 53% of the study area, The Nile: there is about 73 km of the Nile passing through the study area and it is the responsible for the presence of the agricultural and the geological nature (with other effects) of the study area, And two geological Units, Te (Tertiary, which represents sands and sandstones with clay and marl), and Tp (Tertiary

Pliocene, which represents sands, sandstone and gravels), Fig. 11.

In addition, the classification accuracy assessment (CAA) was performed for the obtained results using 327 field reference points with Landsat 7 image (with the same date that the SAR data acquired) Fig. 12 & 13. The CAA has shown the classification accuracy to be around 81.82% with Kappa coefficient of 0.8344, which is acceptable according to Table 1.

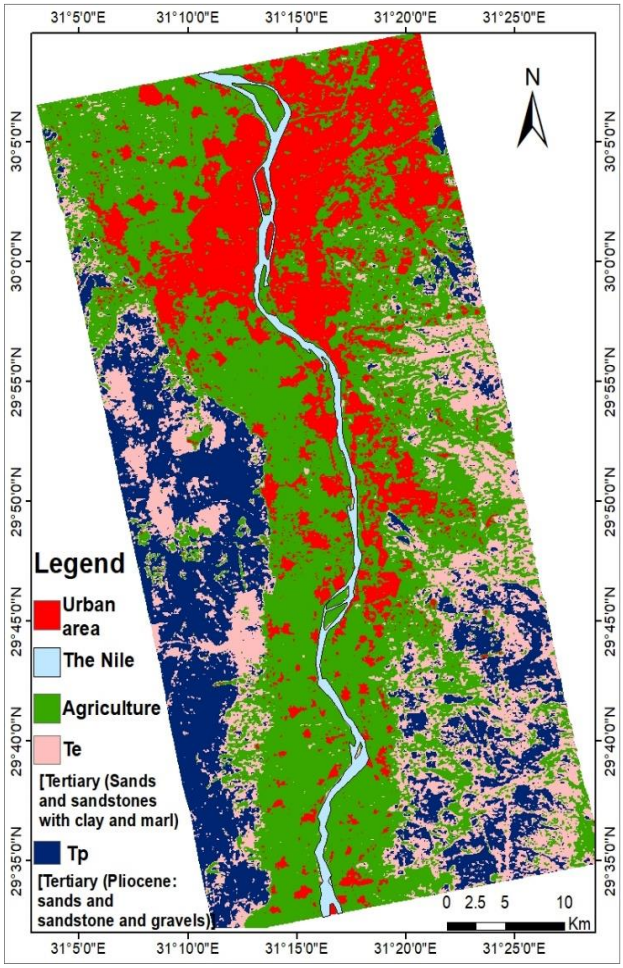

Fig. 11 The resultant classified image

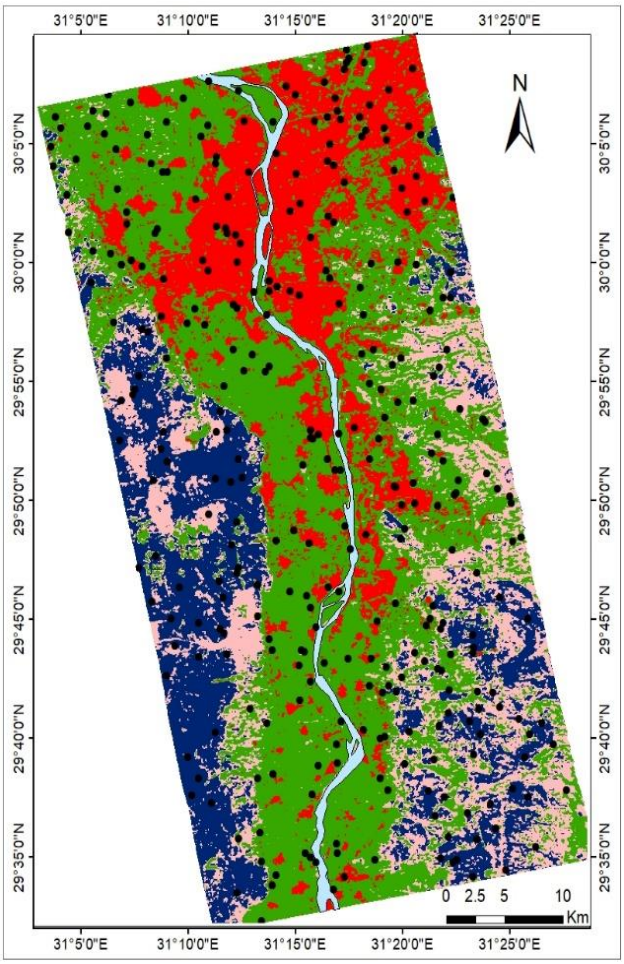

Fig. 12 The accuracy points on the classified image

4. Conclusion

Microwave remote sensing data has recently become popular for land cover/land use classification. This study shows how useful the full-polarimetric ALOS-PALSAR data in mapping the land use / land cover and geology. This paper includes data collection, data interpretation, and a validation tool, as well as methodology and preliminary findings. In the land use, land cover, and geology mapping analysis, the ALOS-PALSAR image was exposed to the supervised classification technique. The nature of the region influenced the selection of the PALSAR data training area. In previous research, the best supervise classifier was selected because it had the highest overall accuracy and kappa coefficient.

using full-polarimetric ALOS/PALSAR data, the land cover and geology of Greater Cairo, Egypt, can be accurately mapped without suffering and wasting time, effort, or facing hazards.

The polarimetric microwave ALOS PALSAR data (Quad mode) is an effective method for classifying various land features from space. In this analysis, the Wishart H-A segmentation classifier with quad mode polarisation microwave and ALOS/PALSAR data provided the highest level of accuracy. Finally, the findings show that integrating the classified targets based on radar scattering response together with their optical reflectance information is effective for discriminating and classifying the land cover and geological units.

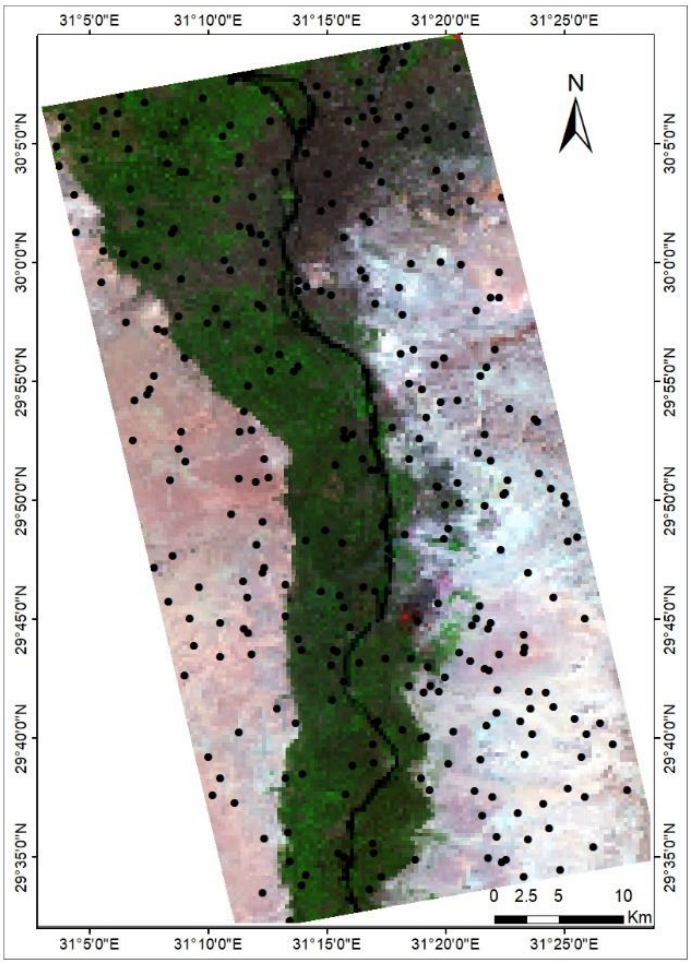

Fig. 13 Landsat 7 image with the accuracy control points

Table **1** Kappa value interpretation [23]

Value	Category
< 0	No agreement
0 – 0.20	Slight
0.21 – 0.40	Fair
0.41 – 0.60	Moderate
0.61 – 0.80	Substantial
0.81 – 1.0	Perfect

5. REFRENCES

1. **Al-Tahir, R., Saeed, I. and Mahabir, R. (2014).** Application of remote sensing and GIS technologies in flood risk management. Flooding and climate change: sectorial impacts and adaptation strategies for the Caribbean region, 137 - 150.
2. **Henderson, F. M., Chasan, R., Portolese, J. and Hart Jr, T. (2002).** Evaluation of SAR-optical imagery synthesis techniques in a complex coastal ecosystem. Photogrammetric Engineering and Remote Sensing, **68**(8): 839 - 846.

3. **Berens, P. (2006).** Introduction to synthetic aperture radar (SAR). FGAN-FHR RESEARCH INST FOR HIGH FREQUENCY PHYSICS AND RADAR TECHNIQUES WACHTBERG (GERMANY).
4. **Sultan, M., Arvidson, R. E. and Sturchio, N. C. (1986).** Mapping of serpentinites in the Eastern Desert of Egypt by using Landsat thematic mapper data. Geology, **14**(12): 995 - 999.
5. **Abrams, M. J., Rothery, D. A. and Pontual, A. (1988).** Mapping in the Oman ophiolite using enhanced Landsat Thematic Mapper images. Tectonophysics, **151**(1-4): 387 - 401.
6. **Jutz, S. L. and Chorowicz, J. (1993).** Geological mapping and detection of oblique extensional structures in the Kenyan Rift Valley with a SPOT/Landsat-TM datamerge. International Journal of Remote Sensing, **14**(9): 1677 - 1688.
7. **Sabins, F. F. (1999).** Remote sensing for mineral exploration. Ore geology reviews, **14**(3-4): 157 - 183.
8. **Singhroy, V. H., Loehr, J. E. and Correa, A. C. (2000)**. Landslide risk assessment with high spatial resolution remote sensing satellite data. In IGARSS 2000. IEEE 2000 International Geoscience and Remote Sensing Symposium. Taking the Pulse of the Planet: The Role of Remote Sensing in Managing the Environment. Proceedings, **6:** 2501 - 2503.
9. **Kruse, F. A., Boardman, J. W. and Huntington, J. F. (2003).** Transactions on Geoscience & Remote Sensing, **41**(6), 1388-1400.
10. **Chipman, J. W., Lillesand, T. M., Schmaltz, J. E., Leale, J. E. and Nordheim, M. J. (2004).** Mapping lake water clarity with Landsat images in Wisconsin, USA. Canadian journal of remote sensing, **30**(1): 1 - 7.
11. **Debba, P., Van Ruitenbeek, F. J. A., Van Der Meer, F. D., Carranza, E. J. M. and Stein, A. (2005).** Optimal field sampling for targeting minerals using hyperspectral data. Remote Sensing of Environment, **99**(4): 373 - 386.
12. **Geiß, C., Taubenböck, H., Wurm, M., Esch, T., Nast, M., Schillings, C. and Blaschke, T. (2011).** Remote sensing-based characterization of settlement structures for assessing local potential of district heat. Remote Sensing, **3**(7): 1447 - 1471.
13. **Amer, R., Kusky, T. and El Mezayen, A. (2012).** Remote sensing detection of gold related alteration zones in Um Rus area, Central Eastern Desert of Egypt. Advances in Space Research, **49**(1): 121 - 134.
14. **Markandeyulu, A., Patra, I., Raju, B. V. S. N., Chaturvedi, A. K. and Parihar, P. S. (2012).** Interpretation of aero-magnetic data and satellite imagery to delineate structure—a case study for uranium exploration from Gwalior Basin, India. Journal of the Geological Society of India, **80**(3): 382 - 392.
15. **Alanazi, H. A. and Ghrefat, H. A. (2013).** Spectral analysis of multispectral Landsat 7 ETM+ and ASTER data for mapping land cover at Qurayah Sabkha, Northern Saudi Arabia. Journal of the Indian Society of Remote Sensing, **41**(4): 833 - 844.
16. **Soulaimani, A., Admou, H., Youbi, N., Hafid, A. and Hefferan, K. P. (2014).** Application of ASTER remote sensing data to geological mapping of basement domains in arid regions: a case study from the Central Anti-Atlas, Iguerda inlier, Morocco. Arabian Journal of Geosciences, **7**(6): 2407 - 2422.
17. **Landis, J. R. and Koch, G. G. (1977).** The measurement of observer agreement for categorical data. biometrics, 159 - 174.
18. **Kruse, F. A., Kim, A. M., Runyon, S. C., Carlisle, S. C., Clasen, C. C., Esterline, C. H. and Olsen, R. C. (2014)**. Multispectral, hyperspectral, and LiDAR remote sensing and geographic information fusion for improved earthquake response. In Algorithms and Technologies for Multispectral, Hyperspectral, and Ultraspectral Imagery. International Society for Optics and Photonics, **9088**: 90880K
19. **Madani, A. and Niyazi, B. (2015).** Groundwater potential mapping using remote sensing techniques and weights of evidence GIS model: a case study from Wadi Yalamlam basin, Makkah Province, Western Saudi Arabia. Environmental Earth Sciences, **74**(6): 5129 - 5142.
20. **Gabr, S. S., Hassan, S. M. and Sadek, M. F. (2015)**. Prospecting for new gold-bearing alteration zones at El-Hoteib area, South Eastern Desert, Egypt, using remote sensing data analysis. Ore Geology Reviews, **71:** 1-13.

21. **Sonbul, A. R., El-Shafei, M. K. and Bishta, A. Z. (2016).** Using remote sensing techniques and field-based structural analysis to explore new gold and associated mineral sites around Al-Hajar mine, Asir terrane, Arabian Shield. Journal of African Earth Sciences, **117:** 285 - 302.
22. **Vural, A., Corumluoglu, Ö. And Asri, I. (2017).** Remote sensing technique for capturing and exploration of mineral deposit sites in Gumushane metallogenic province, NE Turkey. Journal of the Geological Society of India, **90**(5): 628 - 633.
23. **Elachi, C. (1988).** Spaceborne radar remote sensing: applications and techniques. New York.
24. **Saepuloh, A., Koike, K., Urai, M. and Sumantyo, J. T. S. (2015).** Identifying surface materials on an active volcano by deriving dielectric permittivity from polarimetric SAR data. IEEE Geoscience and Remote Sensing Letters, **12**(8): 1620 - 1624.
25. **Feng, G., Jónsson, S. and Klinger, Y. (2017).** Which fault segments ruptured in the 2008 Wenchuan earthquake and which did not? New evidence from near-fault 3D surface displacements derived from SAR image offsets. Bulletin of the Seismological Society of America, **107**(3): 1185 - 1200.
26. **Tseng, K. H., Kuo, C. Y., Lin, T. H., Huang, Z. C., Lin, Y. C., Liao, W. H. and Chen, C. F. (2017).** Reconstruction of time-varying tidal flat topography using optical remote sensing imageries. ISPRS journal of photogrammetry and remote sensing, **131:** 92 - 103.
27. **Ng, A. H. M., Ge, L., Du, Z., Wang, S. and Ma, C. (2017).** Satellite radar interferometry for monitoring subsidence induced by longwall mining activity using Radarsat-2, Sentinel-1 and ALOS-2 data. International journal of applied earth observation and geoinformation, **61:** 92 - 103.
28. **Sun, Y., Jiang, L., Liu, L., Sun, Q., Wang, H. and Hsu, H. (2017).** Mapping glacier elevations and their changes in the western Qilian Mountains, northern Tibetan Plateau, by bistatic InSAR. IEEE Journal of Selected Topics in Applied Earth Observations and Remote Sensing, **11**(1): 68 – 78.
29. **Béjar-Pizarro, M., Carrizo, D., Socquet, A., Armijo, R., Barrientos, S., Bondoux, F. and Vigny, C. (2010).** Asperities and barriers on the seismogenic zone in North Chile: state-of-the-art after the 2007 M w 7.7 Tocopilla earthquake inferred by GPS and InSAR data. Geophysical Journal International, **183**(1): 390 - 406.
30. **Salvi, S., Tolomei, C., Boncori, J. P. M., Pezzo, G., Atzori, S., Antonioli, A. and Coletta, A. (2012).** Activation of the SIGRIS monitoring system for ground deformation mapping during the Emilia 2012 seismic sequence, using COSMO-SkyMed InSAR data. Annals of Geophysics, **55**(4): 970 - 976.
31. **Sun, L. and Muller, J. P. (2014).** Evaluation of the Use of Sub-Pixel Offset Tracking Method to Monitor Landslides in Densely Vegetated Terrain in the Three Gorges Region, China. Dragon 3Mid Term Results, **724:** 112.
32. **Wu, C., Li, X., Chen, W. and Li, X. (2020).** A review of geological applications of high-spatial-resolution remote sensing data. Journal of Circuits, Systems and Computers, **29**(06): 2030006.
33. **Moustafa, A. and Abd-Allah, A. M. (1991).** Structural setting of the central part of the Cairo-Suez district. Earth Sci, **5:** 133 - 145.
34. **Moustafa, A. R., Yehia, M. A. and Abdel Tawab, S. (1985).** Structural setting of the area east of Cairo, Maadi and Helwan. Middle East Res. Centre, Ain Shams Univ., Sci. Res. Series, **5:** 40 - 64.
35. **Said, R. (1962).** The Geology of Egypt. Amsterdam, Elsevier.

36. **Abdeen, M. M., Gaber, A., Shokr, M. and El-Saadawy, O. A. (2018).** Minimizing labeling ambiguity during classification process of the geological units covering the central part of the Suez Canal Corridor, Egypt using their radar scattering response. The Egyptian Journal of Remote Sensing and Space Science, **21:** S55 - S66.
37. **Lee, J. S. and Pottier, E. (2009).** Polarimetric radar imaging: from basics to applications. Optical Science and Engineering.
38. **Congalton, R. G. (2001).** Accuracy assessment and validation of remotely sensed and other spatial information. International Journal of Wildland Fire, **10**(4): 321 - 328.
39. **Cloude, S. R. and Pottier, E. (1996).** A review of target decomposition theorems in radar polarimetry. IEEE transactions on geoscience and remote sensing, **34**(2): 498 - 518.
40. **Cloude, S. R. and Pottier, E. (1997).** An entropy based classification scheme for land applications of polarimetric SAR. IEEE transactions on geoscience and remote sensing, **35**(1): 68 - 78.
41. **Cloude, S. R. and Papathanassiou, K. P. (1998).** Polarimetric SAR interferometry. IEEE Transactions on geoscience and remote sensing, **36**(5): 1551 - 1565.
42. **Cloude, S. R., Pottier, E. and Boerner, W. M. (2002)**. Unsupervised image classification using the entropy/alpha/anisotropy method in radar polarimetry. In NASA-JPL, AIRSAR-02 Workshop, **44(**1334): 04 - 06.
43. **Lu, D. and Weng, Q. (2007).** A survey of image classification methods and techniques for improving classification performance. International Journal of Remote Sensing, 28(5): 823-870.
44. **Cracknell, P. (1998).** Synergy in remote sensing - what' s in a pixel ? International Journal of Remote Sensing, **19**(11): 2025 –2047.
45. **Benz, U. C., Hofmann, P., Willhauck, G., Lingenfelder, I. and Heynen, M. (2004).** Multiresolution, object-oriented fuzzy analysis of remote sensing data for GIS-ready information. ISPRS Journal of Photogrammetry and Remote Sensing, **58**(3-4): 239 – 258.
46. **Wang, L., Sousa, W. P., Gong, P. and Biging, G. S. (2004).** Comparison of IKONOS and QuickBird images for mapping mangrove species on the Caribbean coast of Panama. Remote Sensing of Environment, **91**(3-4): 432 – 440.
47. **Moreira, A., Prats-Iraola, P., Younis, M., Krieger, G., Hajnsek, I. and Papathanassiou, K. P. (2013).** A tutorial on synthetic aperture radar. IEEE Geoscience and remote sensing magazine, **1**(1): 6 - 43.
48. **Campbell, J. B. and Wynne, R. H. (2011).** Introduction to remote sensing. Guilford Press.
49. **Senseman, G. M., Bagley, C. F. and Tweddale, S. A. (1995).** Accuracy Assessment of the Discrete Classification of Remotely-Sensed Digital Data for Landcover Mapping. CONSTRUCTION ENGINEERING RESEARCH LAB (ARMY) CHAMPAIGN IL.
50. **Chen, Y. S. (2019).** Interpretation of Kappa Values: Evaluate the agreement level with condition.